



HAL
open science

Round robin test on angle of repose: DEM simulation results collected from 16 groups around the world

Hidetaka Saomoto, Naotaka Kikkawa, Shuji Moriguchi, Yukio Nakata, Masahide Otsubo, Vasileios Angelidakis, Yi Pik Cheng, Kevin Chew, Gabriele Chiaro, Jérôme Duriez, et al.

► To cite this version:

Hidetaka Saomoto, Naotaka Kikkawa, Shuji Moriguchi, Yukio Nakata, Masahide Otsubo, et al.. Round robin test on angle of repose: DEM simulation results collected from 16 groups around the world. *Soils and Foundations*, 2023, 63 (1), pp.101272. 10.1016/j.sandf.2023.101272 . hal-03985412

HAL Id: hal-03985412

<https://hal.inrae.fr/hal-03985412v1>

Submitted on 13 Feb 2023

HAL is a multi-disciplinary open access archive for the deposit and dissemination of scientific research documents, whether they are published or not. The documents may come from teaching and research institutions in France or abroad, or from public or private research centers.

L'archive ouverte pluridisciplinaire **HAL**, est destinée au dépôt et à la diffusion de documents scientifiques de niveau recherche, publiés ou non, émanant des établissements d'enseignement et de recherche français ou étrangers, des laboratoires publics ou privés.

Author response for reviewers'
comments: S1-S10.

Round robin test on angle of repose: DEM simulation
results collected from 16 groups around the world

Hidetaka Saomoto^{a,*}, Naotaka Kikkawa^b, Shuji Moriguchi^c, Yukio Nakata^d,
Masahide Otsubo^{e,1}, Vasileios Angelidakis^f, Yi Pik Cheng^g, Kevin Chew^h,
Gabriele Chiaro^h, Jérôme Duriezⁱ, Sacha Duvergerⁱ, Joaquín Irazábal
González^j, Mingjing Jiang^{k,2}, Yohei Karasaki^e, Akiko Kono^l, Xintong Li^m,
Zhuyuan Linⁿ, Asen Liu^m, Sadegh Nadimi^f, Hitoshi Nakase^o, Daisuke
Nishiura^p, Utsa Rashique^q, Hiroyuki Shimizu^r, Kumpei Tsuji^s, Takashi
Watanabe^t, Xiaomin Xu^u, Mourad Zeghal^q

^a *Institute of Earthquake and Volcano Geology, National Institute of Advanced Industrial
Science and Technology, Ibaraki, Japan*

^b *Construction Safety Research Group, National Institute of Occupational Safety and
Health, Japan, Tokyo, Japan*

^c *International Research Institute of Disaster Science, Tohoku University, Miyagi, Japan*

^d *Graduate School of Sciences and Technology for Innovation, Yamaguchi
University, Yamaguchi, Japan*

^e *Institute of Industrial Science, The University of Tokyo, Tokyo, Japan*

^f *School of Engineering, Newcastle University, Newcastle upon Tyne, The United
Kingdom*

^g *Department of Civil, Environmental and Geomatic Engineering, University College
London, London, The United Kingdom*

^h *Civil and Natural Resources Engineering, University of Canterbury, Christchurch, New
Zealand*

ⁱ *RECOVER, INRAE, Aix Marseille University, Aix-en-Provence, France*

^j *Machine Learning in Civil Engineering Group, International Centre for Numerical
Methods in Engineering (CIMNE), Barcelona, Spain*

^k *School of Civil Engineering, Suzhou University of Science and Technology, Jiangsu
Province, China*

^l *Railway Dynamics Division, Railway Technical Research Institute, Tokyo, Japan*

^m *School of Civil Engineering, Tianjin University, Tianjin, China*

ⁿ *Department of Earth Science and Engineering, Nanjing University, Jiangsu, China*

^o *Research And Business Incubation Unit, Tokyo Electric Power Services Co., Ltd.
, Tokyo, Japan*

^p *Center for Mathematical Science and Advanced Technology, Japan Agency for
Marine-Earth Science and Technology, Kanagawa, Japan*

*Corresponding author.

Email address: h-saomoto@aist.go.jp (Hidetaka Saomoto)

¹Present affiliation: Public Works Research Institute, Ibaraki, Japan

²Former affiliation: Tianjin University, Tianjin, China

^q *Civil and Environmental Engineering, Rensselaer Polytechnic Institute , New York, The United States of America*

^r *Civil Engineering Design Division, Kajima corporation , Tokyo, Japan*

^s *Department of Civil Engineering, Kyushu University, Fukuoka, Japan*

^t *Disaster Reduction and Environmental Engineering Dept., Kozo Keikaku Engineering Inc. , Tokyo, Japan*

^u *Department of Engineering, Civil Engineering Division, University of Cambridge, Cambridge, The United Kingdom*

Abstract

The round robin test (the simultaneous analysis of the same problem) is a method to investigate the variance and sensitivity of results provided by different analysts for a given problem and the reliability of the particular software used by each group participating in the test. A round robin test has been conducted for the traditional numerical method (e.g., finite difference method), but not yet for the discrete element method (DEM). This paper presents the results of the first ever round robin test on the DEM simulation for the angle of repose, involving 16 groups from around the world using different softwares. Within the scope of this round robin test, most groups reported similar simulation results for the angle of repose that differed only by a few degrees from the average of the experimental values, which was initially concealed from participants. There was also good agreement on the degree of variance of the angle of repose. In addition, this paper revealed the recent trends on the interparticle constitutive models and DEM softwares by considering the reports obtained from the participants.

Keywords: round robin test, discrete element method, angle of repose, validation, particle, 3D printer

1. Introduction

The discrete element method (DEM) was developed in the 1970s (Cundall, 1971; Cundall and Strack, 1979) and has now become a powerful tool for analyzing the complex behavior of geomaterials featuring particulate assemblies subjected to large deformation and fracturing.

One of the most popular applications of DEM in soil mechanics is to simulate soil element tests, such as the triaxial compression test and the direct shear test. One of the important purposes of simulating soil element tests by DEM is to calibrate the parameters of the interparticle constitutive model by fitting the stress-strain curve obtained from the element tests. After parameter adjustment, the relationship between the microstructure properties, such as particle arrangement, to the macroscopic stress-strain relationship can be discussed. Cheng et al. (2003) created particles that can represent particle fragmentation by bonding about 40 spheres together. They simulated a triaxial compression test using about 400 of these crushable particles. Kikkawa et al. (2013) measured elastic wave velocities of chemical-solidified Toyoura sand using a bender element test and then used the test results to determine the elastic stiffness of contacting DEM particles and the bond stiffness bridging DEM particles. Jiang et al. (2015) proposed an interparticle constitutive model that can account for the rolling and twisting between non-spherical particles and conducted triaxial compression simulations incorporating the proposed model using spherical particles. In their simulation model for triaxial compression tests which included methane hydrate particles, Yu et al. (2016) simulated the stress-strain curve by changing the content of methane hydrate particles inside the simulation model. Otsubo and O'Sullivan (2018)

26 conducted elastic wave propagation tests using particles made of borosili-
27 cate glass with controlled surface roughness. These were simulated by a
28 DEM that incorporates an interparticle constitutive model considering sur-
29 face roughness (Otsubo et al., 2017) and discussed the effect of the particle
30 surface roughness on the macroscopic shear stiffness. Chew et al. (2022)
31 conducted DEM simulations for direct shear tests of gravel-rubber mixtures.
32 The gravel and rubber particles were respectively modeled using clamped
33 particles of five different shapes.

34 In addition to the soil element test, the DEM simulations coupled with
35 fluids have been actively studied. Zeghal and El Shamy (2004) simulated
36 liquefaction by coupling DEM with the Navier-Stokes (NS) equations av-
37 eraged through porosity. Yamaguchi et al. (2017) modeled a channel bed
38 with a DEM and simulated the topographic changes in the channel bed
39 caused by water flowing in the channel. Tsuji et al. (2019) attempted to
40 simulate the ground collapse due to the deterioration of sewer pipes using
41 the DEM and the smoothed particle hydrodynamics (SPH) representing the
42 pore fluid phase. Chen et al. (2022) applied a large-scale DEM simulation
43 code (DEPTH) to the underwater mixing process for deep-sea mining with
44 lubrication models.

45 The DEM is applied in engineering to simulate the ballast behavior under
46 rails caused by railroad loads. Because ballast particles are about 5 cm in
47 diameter, a simulation model close to the actual condition can be created by
48 using a high-performance computer. For example, Irazábal et al. (2017) de-
49 termined the parameters of a bounded rolling friction model to simulate bal-
50 last particles with spherical particles through a comparison with experimental

51 results. Kono (2018) modeled the accurate ballast shape by combining the
52 laser measurement and a shape optimization method for clumping proposed
53 by Matsushima and Saomoto (2002). The ballast particles were then sub-
54 jected to DEM analysis and compared with the results of cyclic loading tests.
55 In their analysis of the behaviors of 190,000 ballast particles, Nishiura et al.
56 (2018) used the quadruple discrete element method (QDEM) in which the
57 material parameters are directly determined from the macroscopic viscoelas-
58 tic parameters used in continuum mechanics. In addition to determining
59 ballast behavior, there are other engineering-oriented applications of DEM
60 simulations: slope hazards (Nakase et al., 2017); rockfall protection (Kanno
61 et al., 2021); rock engineering (Duriez et al., 2011; Shimizu et al., 2011; Jiang
62 et al., 2020); and clay deformation (Lin et al., 2021).

63 The DEM simulations in almost all of the DEM applications described
64 above have been validated by a single analysis group using a single software.
65 From this perspective, it is difficult to evaluate the skill of each analyst
66 and to determine the reliability of the software by referring to these studies
67 individually. This brings us to the motivation of our study.

68 Round robin test for traditional numerical methods such as the finite
69 element method have been conducted over the years for different research
70 fields: seismology (Harris et al., 2011, 2018); rock mechanics (Berre et al.,
71 2021); coastal hydrology (Horrillo et al., 2015). These round robin tests
72 indicate that assessing the user-dependency and sensitivity of results and the
73 reliability of each software is extremely important. It should be noted that
74 despite the importance of the round robin test, it has never been implemented
75 for a DEM simulation.

76 We therefore have conducted the first ever round robin test on DEM
77 simulation for the angle of repose (AOR) under the responsibility of the
78 TC105 Japanese domestic committee in the Japanese Geotechnical Society.
79 The objectives of this study are as follows: (1) To clarify the approach taken
80 by the participants of the round robin test to the simulation of the angle
81 of repose; (2) To quantitatively analyze the differences between individual
82 simulation results and experimental results, based on both the average value
83 and the variance; (3) To discuss the relationship between the differences
84 from experiments and the modeling techniques especially for particle shape
85 modeling and interparticle constitutive equation; and (4) To clearly see the
86 current trend in the DEM software.

87 **2. Round robin test for discrete element method**

88 Although the details of the round robin test are found on the website
89 (TC105 Japanese domestic committee, 2020) and Nakata et al. (2022), we
90 summarize and describe that information here for the convenience of the
91 readers.

92 *2.1. Outline of round robin test*

93 Figure 1 shows the outline of the round robin test for the AOR. Using
94 the artificial particles detailed in Section 2.2, the TC105 Japanese committee
95 (test organizer) conducted two types of experiments for the AOR depicted in
96 Section 2.3. After obtaining the experimental results, the committee released
97 the information relating to the particles used in the experiments (material,
98 shape, mechanical properties) and the two experimental conditions required
99 for the DEM simulation to the participating groups via the website (TC105

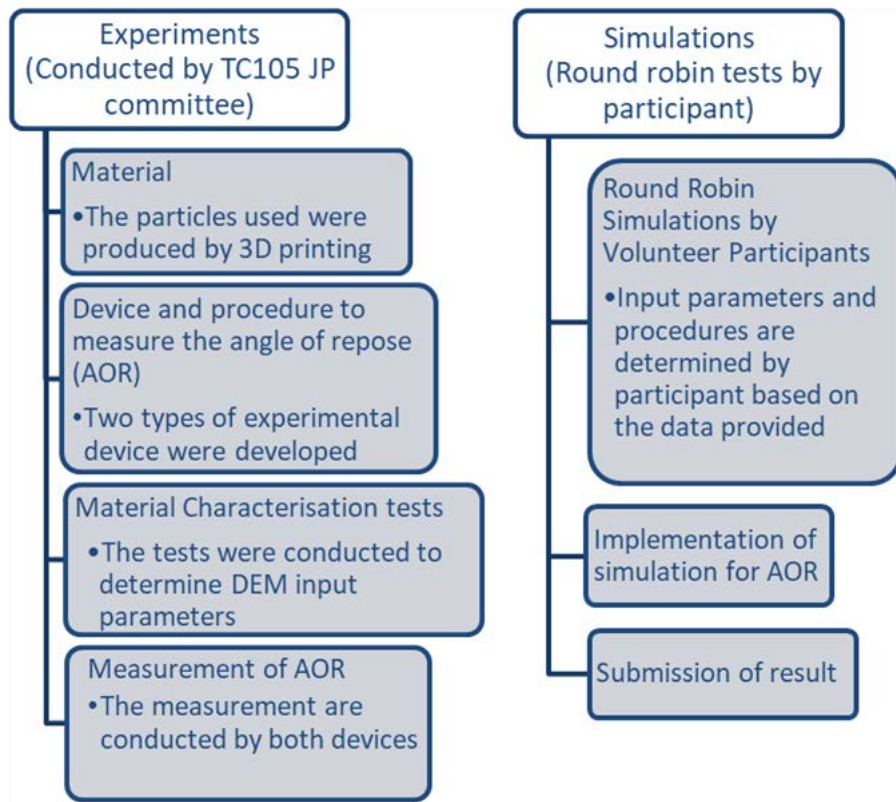


Figure 1: Outline of the round robin test for AOR.

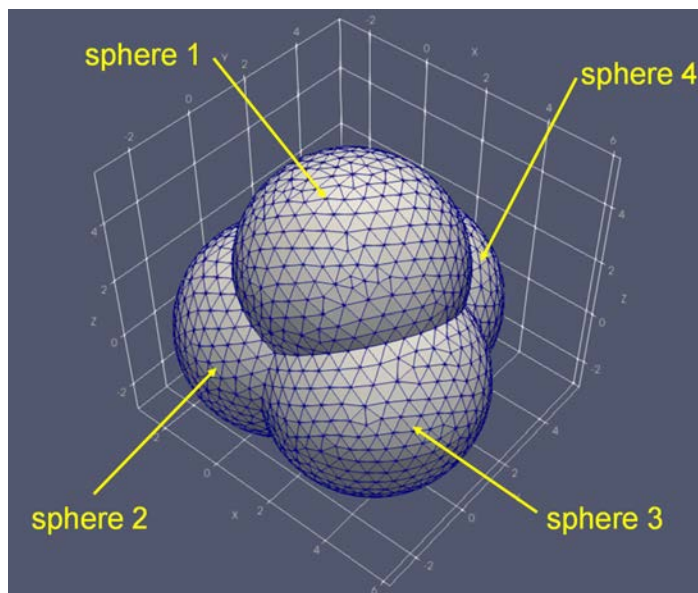


Figure 2: Shape of artificial particles represented by four spheres arranged in a regular tetrahedral form.

100 Japanese domestic committee, 2020). These groups then performed DEM
101 simulations for the experimental conditions based on their research experi-
102 ences and perspectives using the information available on the website and
103 then submitted the simulation results to the committee in accordance with
104 the report format described in Section 2.5.

105 *2.2. Artificial particle used in experiments*

106 Figure 2 shows the shape of the artificial particles, used in the experi-
107 ment. Each artificial particle was designed with four spheres (spheres 1, 2,
108 3, and 4) placed at each vertex of a regular tetrahedron. Note that there is
109 no size distribution for artificial particles used in the experiments. Subse-
110 quently, the artificial particles were realized with resinous material by using
111 a 3D printer. The coordinates of each sphere center are expressed as follows:

Table 1: List of characteristics of the artificial particles.

Parameter	Test	Object	Mean	Standard deviation
Static friction angle	Inclined surface test	Resin-resin	35.5°	3.82°
		Acrylic-resin	27.2°	4.26°
Dynamic friction angle	Inclined surface test	Resin-resin	29.36°	2.42°
		Acrylic-resin	16.5°	7.35°
Coefficient of restitution	Drop test	Resin-resin	0.809	0.0115
		Acrylic-resin	0.790	0.0280
Shear modulus	Cyclic uniaxial test	Resin	560 MPa	158 MPa
		for horizontal plane	680 MPa	70 MPa
		for vertical plane	440 MPa	130 MPa
Normal spring coefficient (Normal contact force: 0.1N)	Cyclic uniaxial test	Resin	6.0×10^4 N/m	1.1×10^4 N/m
		for horizontal plane	6.9×10^4 N/m	0.5×10^4 N/m
		for vertical plane	5.2×10^4 N/m	0.5×10^4 N/m

112 $(0, 0, 0)$, $(3.101, 0, 0)$, $(1.551, 0.895, 2.532)$, and $(1.551, 2.685, 0)$ for spheres 1,
 113 2, 3, and 4, respectively (unit: mm). Note that each sphere has the same
 114 radius (3.101 mm).

115 The material properties of the artificial particles are listed in Table 1.
 116 The mean values and standard deviations of each parameter were obtained
 117 by a sufficient number of experiments. In addition to the information listed
 118 in Table 1, friction angles between the artificial particle material (resin) and
 119 the surface of the experimental apparatus (acrylic plate) have also been mea-
 120 sured (Nakata et al., 2022): static friction angle: 27.2 degrees with the stan-
 121 dard deviation of 4.26 degrees; dynamic friction angle: 16.5 degrees with the
 122 standard deviation of 7.35 degrees.

SS

123 2.3. Two types of AOR experiment

124 The test organizer prepared two types of AOR experimental setup: Device
 125 I is a rectangular type (plane strain condition), as shown in Figure 3, and

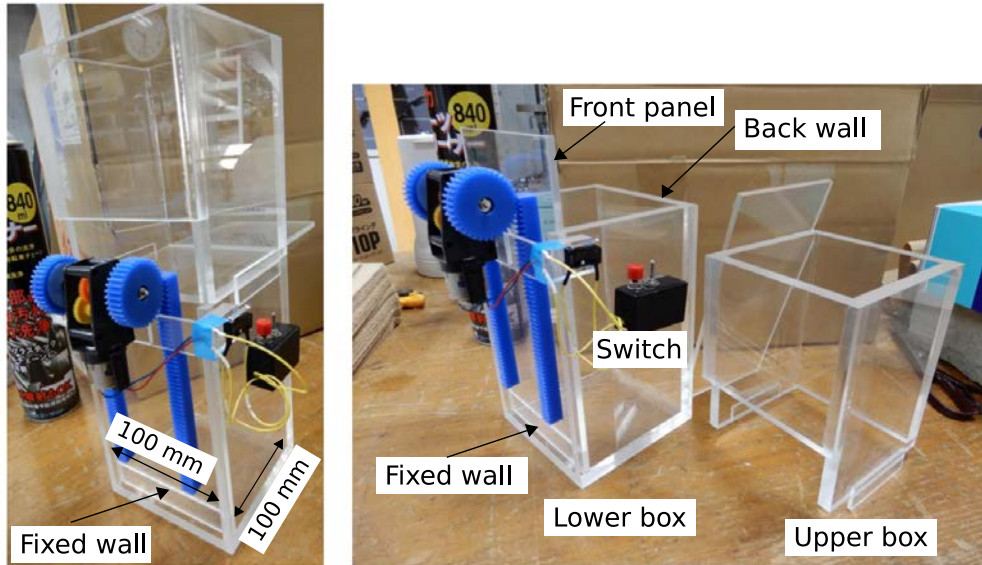


Figure 3: Experimental apparatus for Device I.

126 Device II is a cylindrical type (axial-symmetric condition), as shown in Figure
 127 4.

128 The Device I apparatus is made of transparent acrylic plates and com-
 129 prises an upper and a lower box, separated by a horizontal acrylic plate that
 130 can translate horizontally. The artificial particles (detailed in Section 2.2)
 131 are initially deposited in the upper acrylic box. During the experiment, the
 132 artificial particles firstly fall under the action of gravity by translating the
 133 plate installed between the upper box and the lower box outwards. When
 134 the particles have come to rest, the front panel of the lower box is pulled
 135 upwards by an electric motor at a constant speed of 43 mm/s. Almost 2150
 136 particles were used in those experiment. We can also confirm the size detail
 137 on the website (TC105 Japanese domestic committee, 2020).

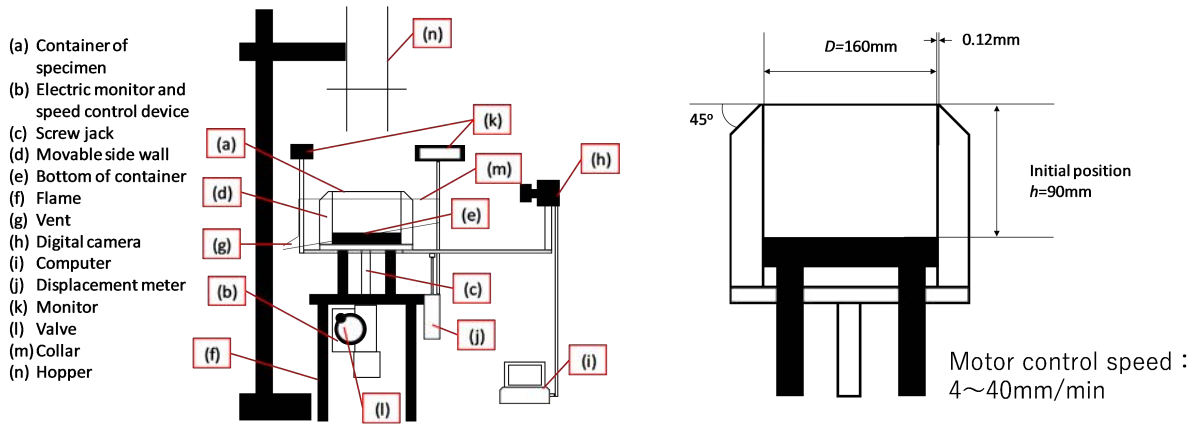


Figure 4: Experimental apparatus for Device II (left: overall view, right: container section where particles are deposited).

138 A schematic illustration of Device II with the cylindrical configuration
 139 is provided in Figure 4. The container in which the particles are placed [a]
 140 is enclosed by an acrylic cylindrical wall [d] and a fixed bottom plate [e]
 141 with a diameter of 160 mm. The cylindrical wall can be moved down at a
 142 constant speed using an electric motor [b], and the initial height from the top
 143 of the cylindrical wall to the bottom plate is 90 mm. Two digital cameras
 144 [h] are placed orthogonally in order to measure the angle of repose. The
 145 experimental procedure for Device II is as follows: (1) the artificial particles
 146 are initially deposited in a hopper of 100 mm diameter; (2) the container [a]
 147 is filled with almost 2700 particles under the action of gravity by translating
 148 the bottom plate of the hopper.

149 The aforementioned experimental procedure was described in detail on
 150 the website (TC105 Japanese domestic committee, 2020) prior to the round
 151 robin test. Therefore, the participants were expected to perform DEM

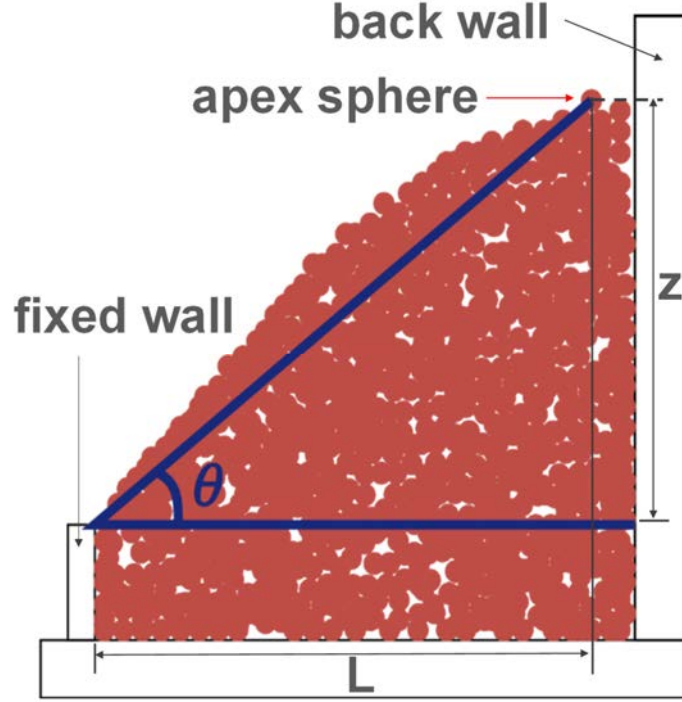


Figure 5: Schematic illustration at the end of DEM simulation for Device I.

152 simulations according to the experimental process for each device.

153 *2.4. AOR measurement in experiment*

154 Figure 5 shows a schematic illustration at the end of the DEM simulation
 155 for Device I. The AOR for Device I is uniquely determined using the coor-
 156 dinate values of the centroid of the apex sphere at the top of the specimen
 157 (Fig. 5). Using lengths Z and L depicted in Figure 5, we have

$$\theta_1 = \tan^{-1} \left(\frac{Z}{L} \right), \quad (1)$$

158 where θ_1 is the AOR for Device I.

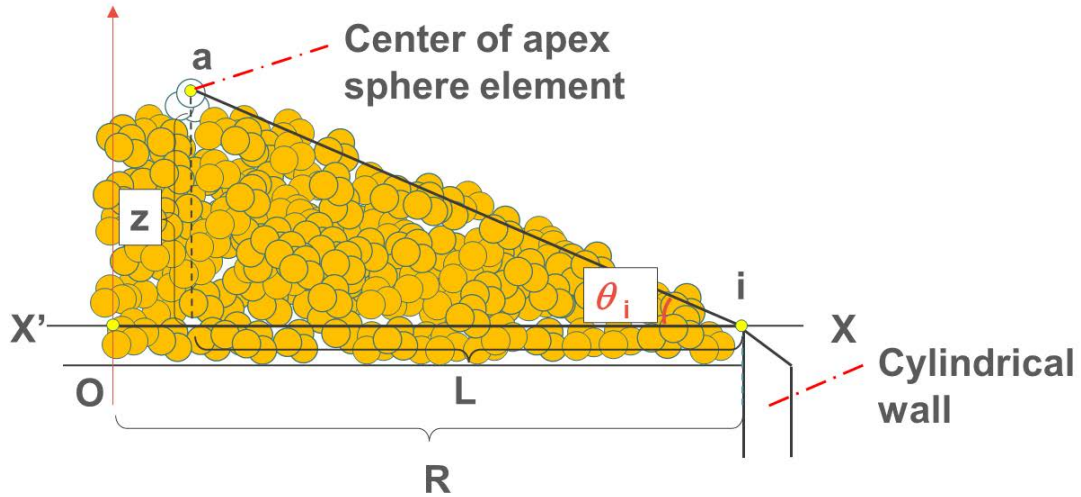


Figure 6: Schematic illustration at the end of DEM simulation for Device II.

159 In the case of Device II, we can use the coordinate values of the apex
 160 sphere of a particle at the end of simulation to determine the AOR, in the
 161 same way as described for Device I. Note that there are several possible
 162 definitions of the AOR for Device II.

163 Figure 6 is a supporting diagram to define the angle of repose in Device
 164 II, indicating a schematic illustration at the end of the DEM simulation for
 165 Device II. In general, the xy-coordinate of the sphere located at the top
 166 (a) does not coincide with the bottom plate center (O). To this end, 360
 167 measuring points were set on the top of the cylindrical wall at intervals of
 168 one degree, and the angle θ_i was calculated for each line connecting each
 169 measuring point (i) and the top of the sphere element (a). Denoting the
 170 maximum θ_i as θ_{\max} and the minimum θ_i as θ_{\min} , the average of these two
 171 values can be a representative of angle of repose for Device II. Here, we

172 employ this definition as the AOR for Device II,

$$\theta_{\text{II}} = \frac{\theta_{\text{max}} + \theta_{\text{min}}}{2}, \quad (2)$$

173 where θ_{II} is the the AOR for Device II. Naturally, Eqs. (1) and (2) are ap-
174 plied to the corresponding DEM simulation results in order to quantitatively
175 compare the simulation results and the experimentally obtained results.

176 It should be noted that the value of AOR generally depends on the initial
177 configuration of particles and subsequent packing characteristics. However,
178 since it is difficult to analyze such effects quantitatively and independently,
179 we tried to compare the experimental data with simulation results based on
180 the concept that the effect is one of the uncertainties which causes variation
181 of the AOR.

S2

182 2.5. Data collection from participants

183 Each participating group is required to submit a spreadsheet containing
184 the predefined questions prepared by the test organizer and the 3D coordi-
185 nates of all sphere particles included in tetrahedral particles at the end of the
186 simulation. The questions in the spreadsheet are designed to gather specific
187 information, including the following: (1) the software used, (2) the parallel
188 computation environment, (3) the interparticle constitutive model and its
189 parameter values, (4) the particle shape and the size used, (5) the method of
190 creating the initial configuration of particles, (6) the setting of the moving
191 speed of the boundary wall, (7) the number of simulation trials.

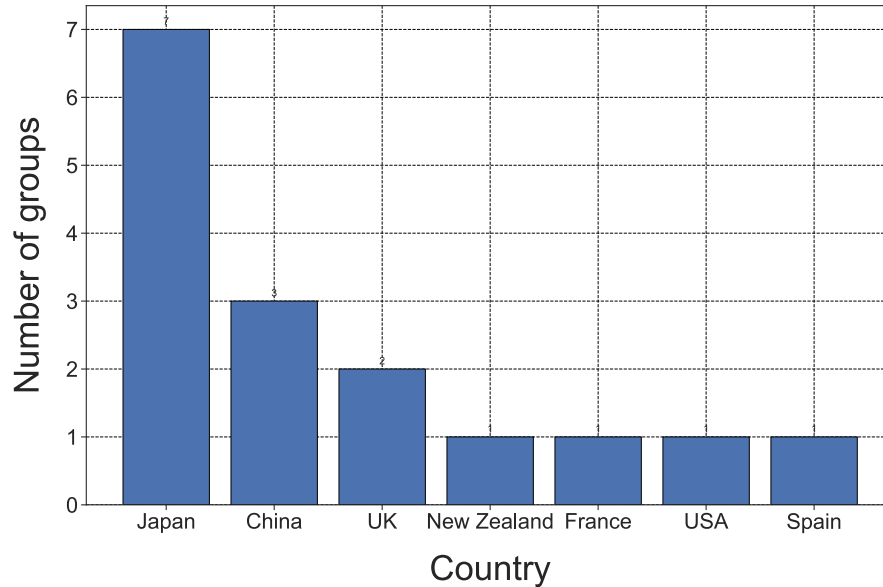


Figure 7: Relationship between the number of analysis groups and country.

192 **3. Results of round robin test**

193 This section summarizes the results of the round robin test where the
 194 reported AOR values are correlated with the adopted input parameters for
 195 each analysis group. It should be noted that the results of the round robin
 196 test are not necessarily general but limited to the specific conditions in the
 197 experiments, such as boundary conditions, artificially-made particles, and
 198 low confining pressure.

51, 56

199 *3.1. Number of participation groups by country*

200 The number of groups who participated in the round robin test by country
 201 is shown in Figure 7. In total, 16 groups from 7 countries participated in the
 202 round robin test. According to Figure 7, Japan has the largest number of

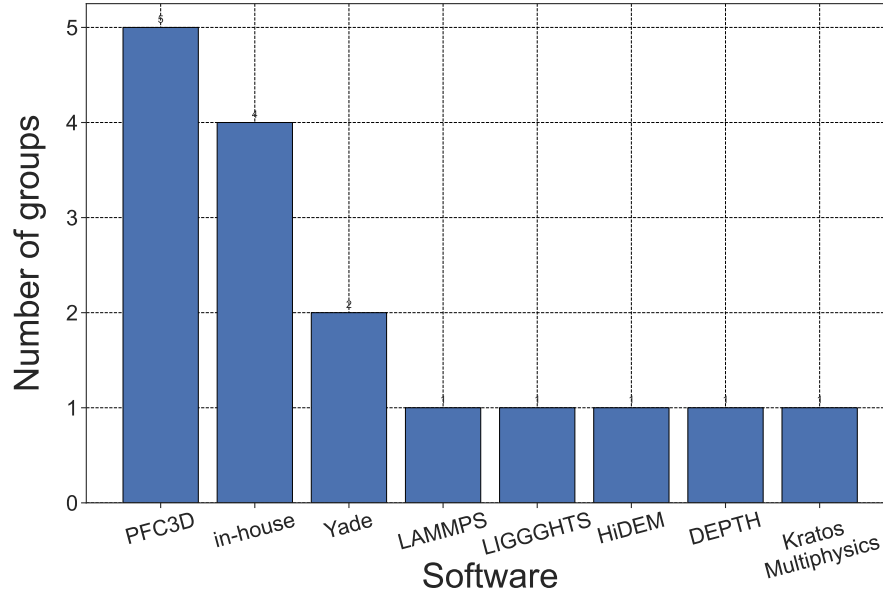


Figure 8: Histogram of software used in round robin test.

203 analysis groups, followed by China and the UK, and France, New Zealand,
 204 Spain, and the United States are represented by an equal number of groups.

205 *3.2. Summary for used software*

206 The statistical results of the software used in the round robin test are
 207 illustrated in Figure 8. It can be seen that software most commonly used
 208 in the round robin test was PFC3D (Itasca Consulting Group, Inc., 2021)
 209 and in-house software. Yade (Smilauer et al., 2021) was used by two groups.
 210 Also, LIGGGHTS (Kloss et al., 2012), LAMMPS (Sandia National Laborato-
 211 ries, 2001; Thompson et al., 2022), HiDEM (Sakaguchi and Nishiura, 2009),
 212 DEPTH(Chen et al., 2020; Nishiura et al., 2021), and Kratos Multiphysics
 213 (Dadvand et al., 2010, 2013) were all used by one group.

214 A brief introduction to the various software chosen for the assigned task

215 follows. The PFC3D is a prominent commercial software manufactured by
216 ITASCA Consulting Group, Inc. and is widely used in discrete element
217 simulations in the field of geotechnical engineering.

218 Most in-house software is developed independently in university labora-
219 tories. Note that we did not investigate the details of them used in the round
220 robin test.

221 Yade is an open-source framework for DEM simulations. Although the
222 core computation parts are written in C++, the user interface is prepared
223 with the Python language for easy handling.

224 LIGGGHTS is an open-source discrete element simulator and is an ex-
225 tension of the molecular dynamics software, LAMMPS (described below). In
226 comparison with LAMMPS, LIGGGHTS has the following additional fea-
227 tures: CAD geometry handling, heat conduction, contact force formulation,
228 and particle arrangement using 3-D meshes.

229 LAMMPS is a classical molecular dynamics simulation code (open-source).
230 While LAMMPS is designed for molecular dynamics simulations, it comes
231 with an original granular mechanics package which is to be distinguished
232 from LIGGGHTS.

233 HiDEM is a Fortran 90/95 based commercial software developed by Japan
234 Agency for Marine-Earth Science and Technology (JAMSTEC). Further-
235 more, DEPTH is a commercial software developed from HiDEM that imple-
236 ments an iterative dynamic load balancer algorithms (Furuichi et al., 2017)
237 enabling it to run the world’s largest-scale DEM simulation on the massive
238 parallel computer systems.

239 KRATOS Multiphysics is an open-source framework for building parallel,

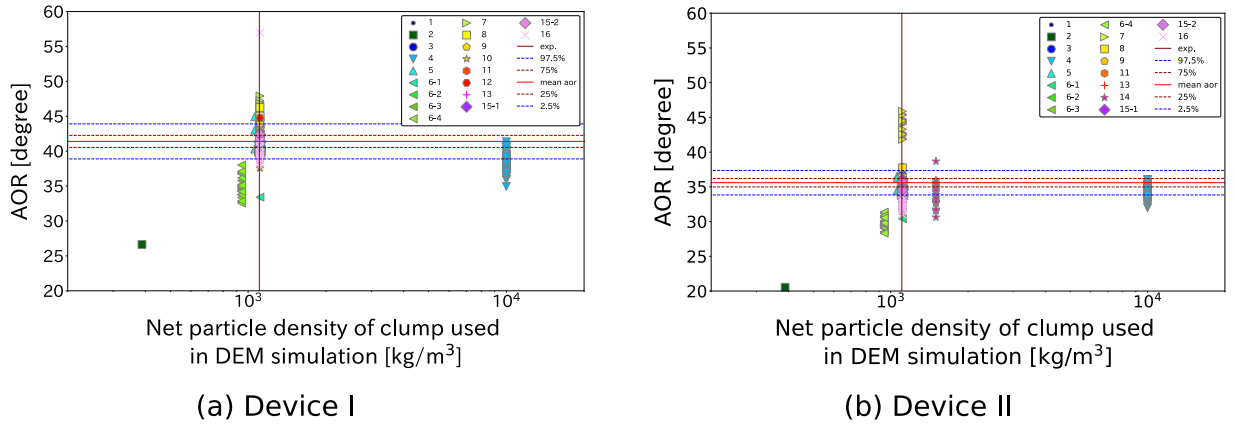


Figure 9: Relationship between AOR experiment results and net particle density used in DEM simulations.

240 multi-disciplinary simulation software including the discrete element method.
 241 This software features easy coupling of the DEM with other analysis tools
 242 implemented in KRATOS, such as the DEM and a fluid analysis or the DEM
 243 and a finite element solid analysis.

244 3.3. Modeling for particle shape and mass

245 Figure 9 shows the relationship between the AOR and the density of the
 246 clumped particle for both Device I (Fig. 9 (a)) and Device II (Fig. 9 (b)).
 247 In Fig. 9, the vertical axis indicates the value of the angle of repose and the
 248 horizontal axis indicates the density used in the DEM simulations. The solid
 249 red line drawn horizontally represents the mean of the experimental AOR
 250 values, and the dashed darkred and blue lines represent the 75% and 97.5%
 251 quartiles, respectively. The vertical line with a density close to 10^3 indicates
 252 the density of the material of particles used in the experiments (1111 kg/m^3).
 253 Each plot shows the AOR calculated from the DEM simulation results sub-
 254 mitted by the participants, and the legend indicates the analyst ID (16 groups

255 in total), respectively. Note that the experimental value (1111 kg/m^2) was
256 employed in 91% of the total number of simulation runs for Device I (350
257 runs in total) and in 87% of the total number of simulation runs for Device
258 II (343 runs in total).

259 Most of the analysis groups used tetrahedron-shaped particles by clump-
260 ing four spheres as in the experiment, while the particles used by several
261 other analysis groups had their own user-defined shape or were spherical.
262 When using a spherical particle shape, which differs from the experimental
263 one, it is necessary to adjust the interparticle constitutive model reflecting
264 the particle shape effect which is equivalent to the experimental state in
265 terms of the rotational motion of the particles and the porosity ratio of the
266 particle assembly. For example, analysis group 14 used spherical particles
267 and introduced the rolling resistance of spherical particles to account for the
268 effect of particle shape. Most analysis groups used the same size particles as
269 those in the experiment.

270 From the perspective of accuracy, most of the simulation results fell within
271 the 97.5% quantile of the AOR obtained from the experiments (assuming
272 normal distribution) irrespective of the device type. Some simulation results
273 deviated from the experimental values (analysis groups 2 and 4 for Device
274 I, and analysis groups 2, 4, and 7 for Device II), but these are basically
275 due to inappropriate parameter settings, **which will be discussed in a later**
276 **section**. In the case of analysis group 6, the AOR recorded from the DEM
277 simulations was smaller than the experimental value, because rounded convex
278 tetrahedral potential particles were employed. These particles interlocked less
279 than the real, concave tetrahedral particles, a behavior that was expected.

← S4

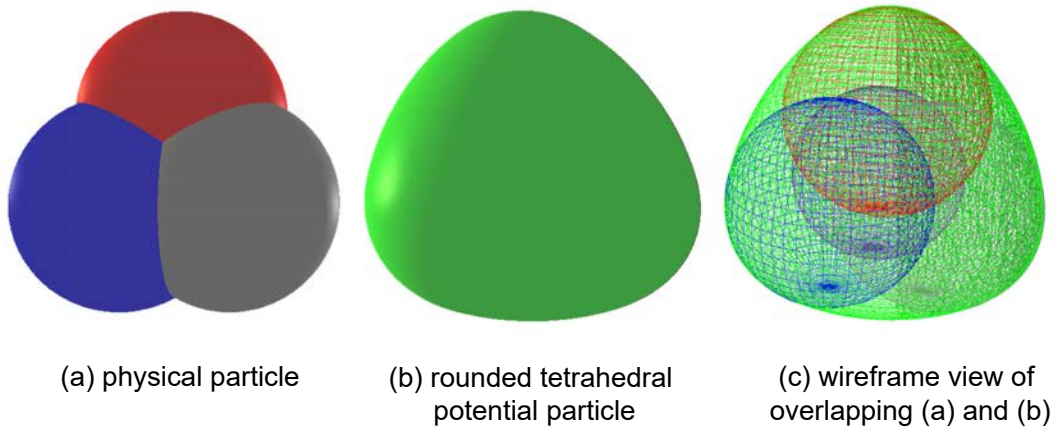


Figure 10: Rounded tetrahedral potential particle shape modeled by analyst 6.

280 Nevertheless, this modeling approach provided a quantification of the effect
 281 that convexity has on the interlocking capabilities of the analyzed material.
 282 There were two cases in which the values of density were significantly different
 283 from the experimental values: analysis group 2, with about 300 kg/m^3 and
 284 analysis group 4, with $10,000 \text{ kg/m}^3$. The authors guess the analysis group 4
 285 may aim to reduce the computational cost by increasing the time step in the
 286 DEM simulation, whereas the intention of group 2 is unclear. The details of
 287 the inappropriate settings are described in the following discussion section.

S5

288 In the case where the density is set to a slightly smaller value (analy-
 289 sis group 6) than the experimental value, it seems that the volume of the
 290 user-defined particle shape (rounded tetrahedral potential particle shape) il-
 291 lustrated in Figure 10 slightly differs from that of the particles used in the
 292 experiment, to approximate closely the real inertial characteristics (mass and
 293 inertia) of the physical particle.

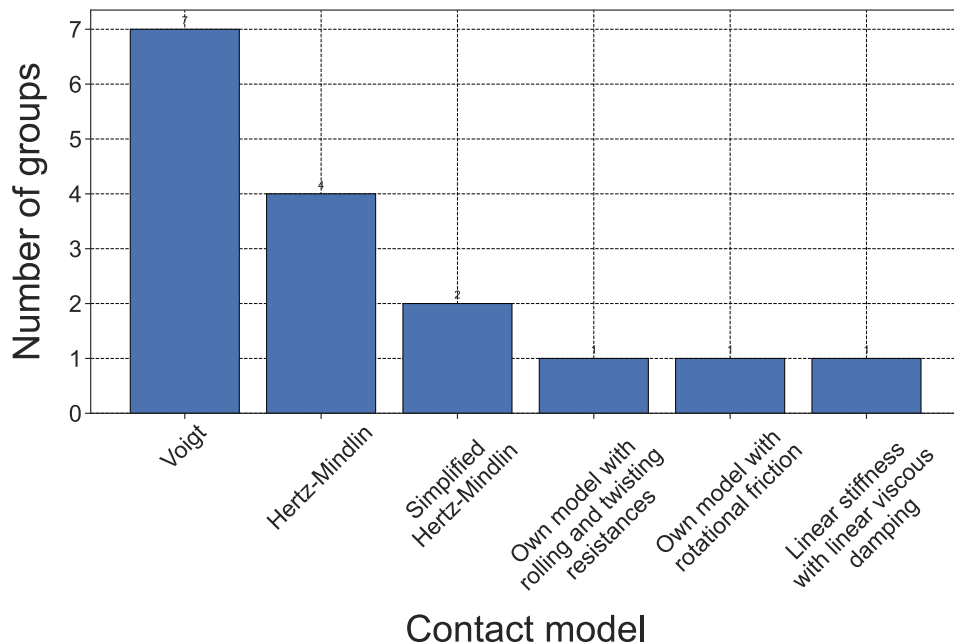


Figure 11: Histogram of interparticle constitutive model.

294 *3.4. Summary for interparticle constitutive model and simulation time step*

295 Figure 11 indicates the histogram of the interparticle constitutive model
 296 used by the analysis groups. The most-used interparticle constitutive model
 297 was the Voigt model, followed by the Hertz-Mindlin model. Most of the
 298 groups that used particles with the same shape as the tetrahedral particle
 299 used in the experiment adopted the Voigt model or the Hertz-Mindlin model.
 300 Meanwhile, the groups that used spherical particles adopted interparticle
 301 constitutive models incorporating rotation resistance corresponding to the
 302 particle shape effect.

303 Since all the constitutive equations require normal stiffness, we first check
 304 the setting of the normal stiffness. In addition, because normal directional

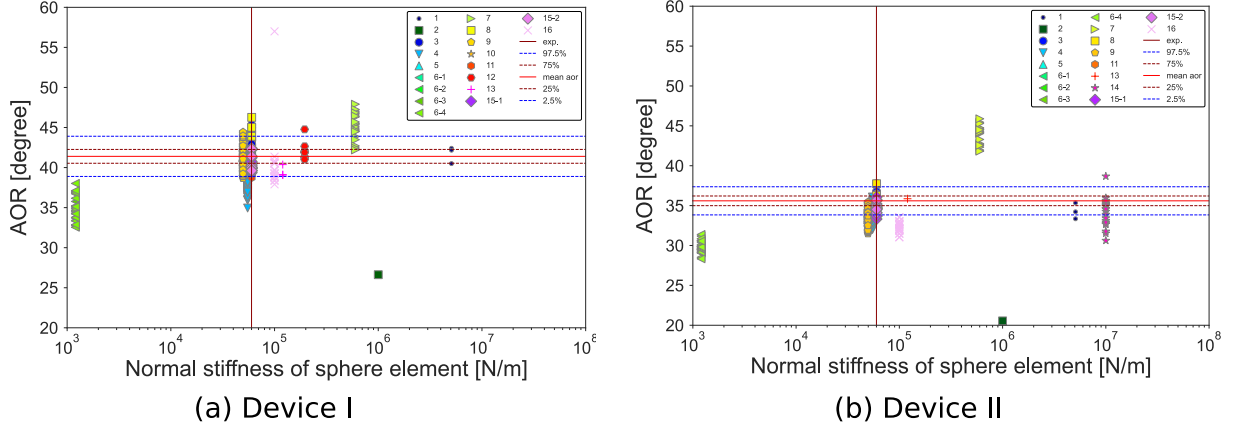


Figure 12: Relationships between AOR experiment results and normal stiffness used in DEM simulations.

305 stiffness is related to the time step setting, normal stiffness is an important
 306 parameter in this sense.

307 Figure 12 shows the relationships between the AOR and the normal stiff-
 308 ness for both Device I (Fig. 12 (a)) and Device II (Fig. 12 (b)). The
 309 horizontal axis shows the normal stiffness used in the DEM simulations. The
 310 meanings of the vertical axis and legend are the same as described in Fig. 9.
 311 The normal stiffness for the Hertz-Mindlin contact model varies non-linearly
 312 with the applied normal force (F_n) or overlap (δ_n) between two sphere ele-
 313 ments in contact. Considering the height of sample ($\simeq 0.1$ m) and the mate-
 314 rial density (1111 kg/m^3), a representative normal force of 0.1 N was used to
 315 estimate the secant normal stiffness (K_n) using the following expression:

$$K_n = \frac{F_n}{\delta_n} = \frac{2}{3} (6E^* R^*)^{\frac{1}{3}} F_n^{\frac{1}{3}}, \quad (3)$$

316 where E^* is the equivalent Young's modulus, and R^* is the effective radius.

317 The definitions for E^* and R^* are respectively as follows:

$$\frac{1}{E^*} = \frac{1 - \nu_i^2}{E_i} + \frac{1 - \nu_j^2}{E_j}, \quad (4)$$

$$\frac{1}{R^*} = \frac{1}{R_i} + \frac{1}{R_j}, \quad (5)$$

318 where E is the Young's modulus, R is the radius, and ν is the Poisson's
 319 ratio of the two contacting sphere elements of i and j . It is noteworthy that
 320 the setting of the normal stiffness (K_n) varies widely among the analysis
 321 groups irrespective of the device type, ranging from the order of 1×10^3 N/m
 322 to 1×10^7 N/m. Although there is a large order of magnitude difference
 323 in the normal stiffness, most of the simulation results fell within the 97.5%
 324 quantile in the AOR comparison, regardless of the device type. This result
 325 suggests that the difference in the normal stiffness may not be so critical to
 326 the AOR. As the normal stiffness relates the time step of the DEM simulation
 327 in conjunction with the mass/density of the particle, we also need to check
 328 the time step used in each simulation run.

329 Figure 13 shows the relationships between the AOR and the normalized
 330 time step for both Device I and Device II. The normalized time step (hori-
 331 zontal axis) is a dimensionless quantity defined by $\frac{\Delta t}{\Delta t_{cr}}$, where Δt is the time
 332 step used in the DEM simulation and Δt_{cr} is a critical time step characterized
 333 by the particle mass M and the normal stiffness K_n ($\Delta t_{cr} = \sqrt{\frac{M}{K_n}}$). Note
 334 that the Δt settings used by each analyst were set in the range of 10^{-6} (s)
 335 to 10^{-4} (s). Most of the DEM simulations were performed with lower values
 336 of the time step than the critical time step, whereas analysis groups 1 and 2
 337 used a large time step that exceeded the critical time step. Almost all the
 338 analysis groups set Δt within the range of 0.01 to 1.0 times of Δt_{cr} . This

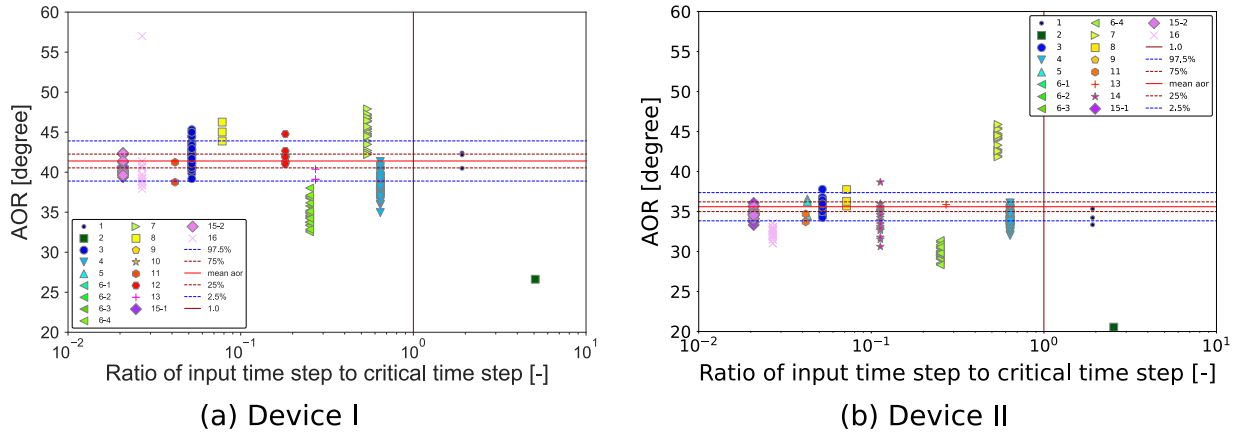


Figure 13: Relationship between AOR experiment results and the normalized time step using the critical time step.

339 suggests that their aim was to improve computational efficiency by setting
 340 as large a time step as possible while ensuring stable simulation.

341 3.5. Summary for friction angle at contact point

342 Figure 14 shows the relationship between the results of the AOR experi-
 343 ment (on the vertical axis) and the setting of the friction angle at the contact
 344 point configured by each analysis group (on the horizontal axis). For both
 345 devices, most of the analysis groups used the interparticle friction coefficient
 346 corresponding to the mean value of the experiment given as prior informa-
 347 tion, as listed in Table 1 ($\tan 35.5^\circ = 0.71$). One of the analysis group set
 348 the interparticle friction coefficient close to 0.5, which may be assumed to be
 349 the friction angle between the acrylic plate and the resin ($\tan 27.2^\circ = 0.51$)
 350 rather than the experimental value of the interparticle friction angle. The
 351 intermediate value close to 0.55 corresponds to the mean value of the dy-
 352 namic friction coefficient obtained from the experiment ($\tan 29.36^\circ = 0.56$).

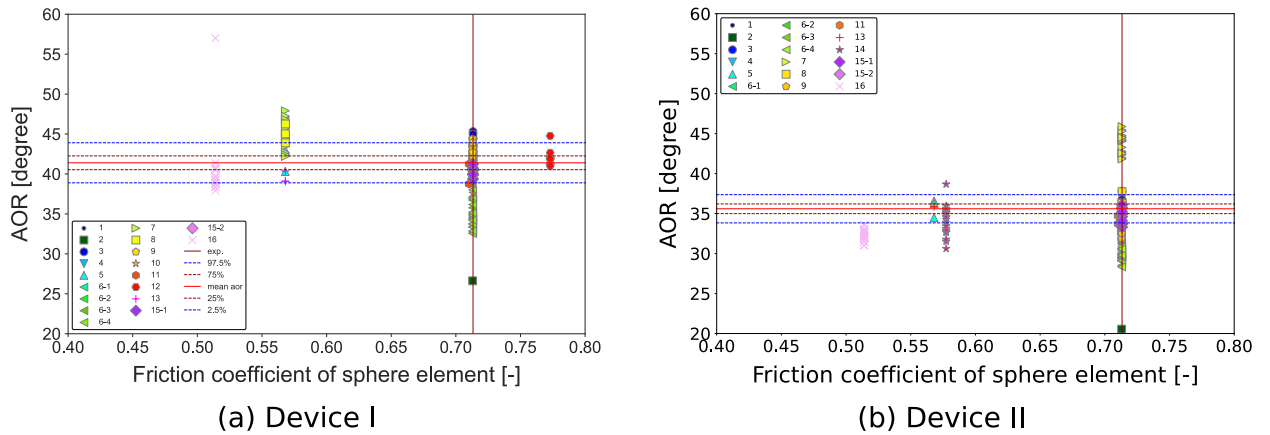


Figure 14: Relationships between AOR experiment results and the friction angle at the contact point used in DEM simulations.

353 It should be noted that while we can find various values for the interparticle
 354 friction angle, all of them have a certain level of accuracy in terms of corre-
 355 spondence with the experimental results. For example, the use of a friction
 356 angle of 0.51 for the interparticle friction angle resulted in no significant dis-
 357 crepancy with the experimental results irrespective of the device type. This
 358 fact suggests that a certain level of particle shape modeling, correct parti-
 359 cle physical properties, and appropriate boundary conditions result in good
 360 predictions of AOR. The initial configuration of the artificial particles differs
 361 from each group, but given the small variation in the results, we believe that
 362 the effect of the initial configuration is small in this round robin test.

57

363 3.6. Comparison with variability between DEM simulations and experiments

364 We compare the results obtained from both the DEM simulations and
 365 the experiments considering the mean and the variations of the AOR. Note
 366 that this comparison is possible because we imposed a certain number of

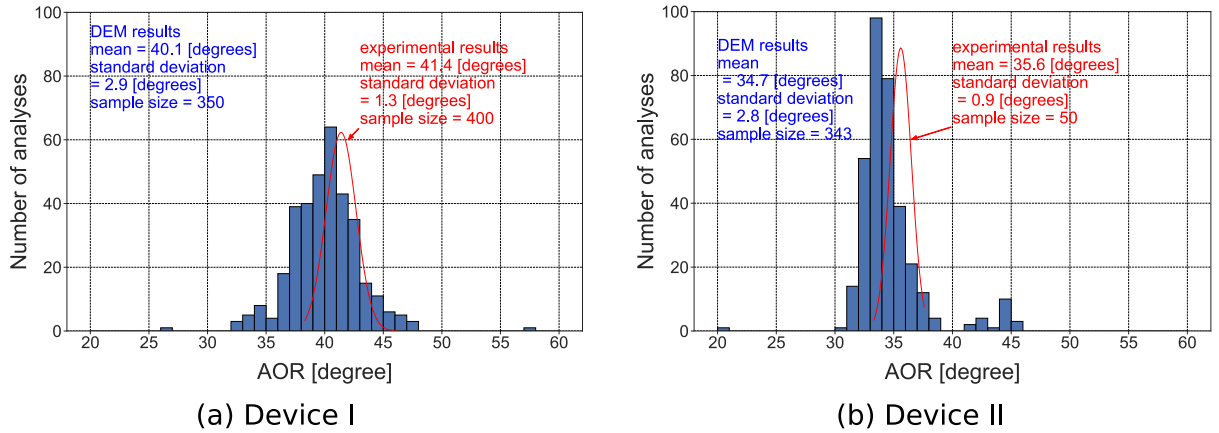


Figure 15: Histogram of AOR based on all simulation results.

367 trials on both the experiments and DEM simulations. Figure 15 indicates
 368 the histograms of AOR (bar plot) using all DEM simulation results for both
 369 Device I and Device II. As for Device I (Fig. 15(a)), the mean and standard
 370 deviation of the histogram (350 samples) are 40.1 degrees and 2.9 degrees,
 371 respectively, from a normal distribution approximating the histogram. Also,
 372 the red solid line shows a normal distribution with a mean of 41.4 degrees
 373 and a standard deviation of 1.3 degrees obtained from the experimental re-
 374 sults (400 samples). Although the histogram shows a few outliers around 26
 375 degrees and 57 degrees, it can be seen that the DEM results simulate the
 376 experimental results with considerable accuracy. In particular, the difference
 377 between the mean values is 1.3 degrees, indicating that the predictions are
 378 remarkably accurate. The variance of the DEM simulations is larger than the
 379 experimental results, but this can be attributed to the normal distribution,
 380 including the outliers.

381 Likewise, the DEM results for Device II have a mean value of 34.7 degrees
 382 and a standard deviation of 2.8 degrees, and the corresponding experimental

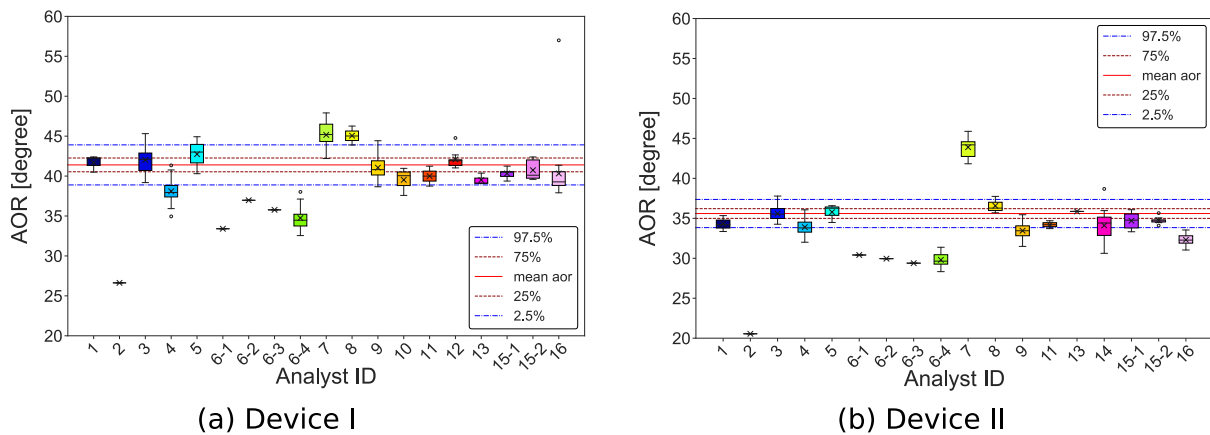


Figure 16: Box plot of AOR simulation results for each participant.

383 values are 35.6 degrees and 0.9 degrees, respectively (Fig. 15(b)). The his-
 384 togram has a bimodal shape with a small peak around 45 degrees, but the
 385 reasons for calculating an AOR greater than 40 degrees are largely due to
 386 the usage of the interparticle constitutive model with an excessive setting for
 387 rotational resistance.

388 4. Discussion

389 The DEM simulation results submitted by 16 groups from 7 countries
 390 were classified and statistically analyzed, and most of the simulation results
 391 were in good agreement with the experimental results. In this section, we
 392 consider the reason for the outliers from the perspective of the parameter
 393 settings. After identifying the causes of outliers, we discuss trends in DEM
 394 software.

395 Figure 16 shows a side-by-side comparison of the DEM simulation results
 396 for each analysis group (16 groups in total), and the variation of each set of
 397 DEM simulation results is also represented using a box plot. The horizontal

398 axis indicates the participating group (analysis group) ID and the vertical
399 axis is the AOR value. The meanings of the solid and dotted lines are the
400 same as those depicted in Fig. 9. Note that the conventions of the box plot
401 can be found in Appendix A: they consist of the 25th percentile, the 50th
402 percentile, the 75th percentile, and outliers.

403 In the case of Device I (Fig. 16(a)), it can be seen that the mean AOR
404 values submitted by the five analysis groups (ID: 2, 4, 6, 7, 8) are located
405 outside the 97.5 percentile. In the five cases with outlier results, we can identify
406 clear reasons for such outlier results in terms of parameter settings, using
407 convex particle shapes and usage of the interparticle constitutive equations.
408 The time step used by analysis group 2 is significantly large, as shown in Fig.
409 13. Due to the use of such a large time step, it can be inferred that a large
410 penetration occurs at the contact point, thereby resulting in a small value
411 of the AOR. The particle density used by analysis group 4 is markedly large
412 (10,000 kg/m³), as shown in Fig. 9. Due to the use of large density, it can be
413 inferred that a large penetration occurs at the contact point, thereby result-
414 ing in a small value of the AOR. The convex, rounded shape of the potential
415 particle used by analysis group 6, illustrated in Fig. 10, is likely the reason
416 for the small value of AOR, as convex particles interlock less than the real,
417 concave ones. Both analysis groups 7 and 8 used the interparticle constitu-
418 tive model with rotation stiffness while they employed tetrahedral particles
419 like those used in the experiment. This result in excessive moment transfer,
420 which leads to a relatively high AOR. It should be noted that the number
421 of simulation runs for analysis groups 2 and 4 is only one, respectively. It
422 is possible that the mean AOR value of the simulation may approach the

← JS

423 experimental one with a larger number of simulations.

424 In the case of Device II (Fig. 16(b)), it can be seen that the mean AOR
425 values submitted by the four analysis groups (ID: 2, 6, 7, 16) are located
426 outside the 97.5 percentile. For analysis groups 2 and 7, the reason is likely
427 the same as that explained for Device I: parameter setting. For analysis group
428 6, the reason is also likely the same as that explained for Device I: particle
429 shape (Fig. 10). However, we could not find the reason for the outlier results
430 of analysis group 16. They used the same interparticle constitutive model
431 with the parameter set that were used in Device I.

432 From the comparison between the DEM simulations and the experimental
433 results, it was confirmed that most of the analysis groups calculated AOR
434 values which were comparable to the experimental results irrespective of the
435 choice of the interparticle constitutive model. There were three trends in
436 the interparticle constitutive model: the Voigt model, the Hertz-Mindlin
437 model and the model with rotational resistance. Most parameters of the first
438 two models provided as prior information listed in Table 1, meanwhile no
439 information is available for the models incorporating rotational resistance.

59

440 It should be noted that the difference in the angle of repose between
441 these models could not be clearly distinguished. Although there were large
442 differences in the normal stiffness individually, most analysis groups used
443 appropriate time steps that stabilized the calculations irrespective of the
444 magnitude of the normal stiffness and particle density. Normal stiffness is of-
445 ten empirically set to a value different from the measured value, which may
446 lead to confusion for beginners. The treatise on DEM (O'Sullivan, 2011)
447 notes that the contact between DEM particles is idealized, and it is difficult

448 to determine the linear stiffness directly from the stiffness of the actual ma-
449 terial. The treatise also argues that linear stiffness should conceptually be
450 considered as a kind of “penalty spring”. While the significant difference in
451 normal stiffness was fortunately not a problem for the prediction of the angle
452 of repose, the exact normal stiffness should be used for a task like accurately
453 predicting the elastic wave velocity.

454 As confirmed by our round robin tests, the parameter settings in DEM
455 simulations are empirical, especially in normal stiffness. It is therefore useful
456 to establish an expert system or a flowchart for parameter setting in the DEM
457 simulations. Interestingly, most of the analysis groups did not consider the
458 standard deviation of each physical property shown in Table 1 when setting
459 those parameters even though there are certain deviations in the AOR values
460 from the DEM simulations. This implies that the variation in the particle
461 configuration had a greater effect on the angle of repose than the variation
462 in the physical properties.

463 This round robin test allowed us to consider the trend in DEM software.
464 We found that the use of PFC3D or in-house software is relatively frequent.
465 Moreover, we found that powerful open source DEM software was also used
466 (Yade, LIGGGHTS, LAMMPS, Kratos). When introducing DEM software,
467 ease of installation, documentation, richness of functions, and ease of use
468 are important considerations, and it was determined that the open source
469 software listed here meets these criteria. In addition to the popularization
470 of powerful DEM software, developing software specializing in particle shape
471 modeling (e.g., Angelidakis et al. (2021)) further promotes the use of DEM
472 in various engineering fields.

473 Through these round robin tests for the angle of repose, it is reconfirmed
474 that the parameter settings of the interparticle constitutive model and the
475 settings of time increments are extremely important. To increase the relia-
476 bility of DEM analysis, it is necessary to steadily accumulate knowledge on
477 parameter settings. We believe that these activities will lead to the establish-
478 ment of verification and validation (V&V) guidelines for DEM simulations.
479 Finally, we touch on the prospects for future round robin tests in terms of the
480 problem settings. There are requests to conduct triaxial compression tests
481 with a certain level of confining pressure, but the problem settings should be
482 decided carefully, considering the difficulty of the experiment and the abilities
483 of many software packages to be used in the round robin test.

S/O

484 5. Conclusions

485 According to the tabulation of the DEM simulation results for two types
486 of experimental settings, most simulation cases submitted by participants
487 agreed with the experimental results with a certain level of accuracy in both
488 average and variance values for the angle of repose, irrespective of the types
489 of experiment. For a few cases where the discrepancy with the experimental
490 results was large, it was concluded that this discrepancy was attributed to
491 the selected values of modeling parameters, and to the employed modeling
492 approach (i.e. clumps versus rounded convex particles). In other words, most
493 of the software used in the round robin test works correctly providing the
494 proper parameter settings are used. The collected data also revealed trends in
495 the selection of the interparticle constitutive model (Voigt and Hertz-Mindlin
496 models) and the DEM software (PFC3D, in-house, and Yade).

497 In future work, we will continue to conduct worldwide DEM round robin
498 tests under the handling of the TC105 Japanese domestic committee to en-
499 sure the accuracy of the DEM simulations and the reliability of each type of
500 DEM software.

501 Appendix A. Box plot notation

502 Figure A.1 shows the details of the box plot notation used in Fig 16.
503 In general, the median differs from the mean and is less sensitive to out-
504 liers. Hence, the median is useful when the data does not obey the normal
distribution.

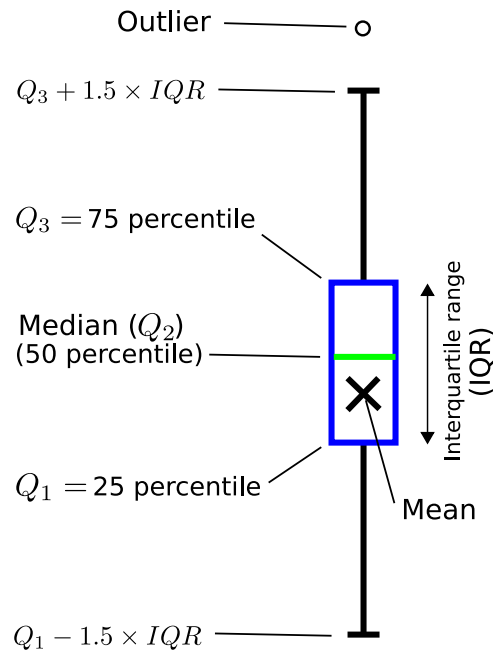


Figure A.1: Box plot notation.

505

506 **Acknowledgement**

507 We would like to thank Professor Catherine O’Sullivan of the Imperial
508 College London for providing us with materials on an example for DEM ver-
509 ification. We also would like to express our appreciation to the participants
510 for their cooperation: Assoc. Prof. Mitsuteru Asai of Kyushu University;
511 Dr. Stéphane Bonelli of INRAE Aix Marseille University; Mr. Yu Hirano
512 of the University of Tokyo; Mr. Ryoh Kuramoto of Kozo Keikaku Engineer-
513 ing Inc.; Prof. Takashi Matsushima of University of Tsukuba; Dr. Shintaro
514 Ohno of Kajima corporation; Dr. Pierre Philippe of INRAE Aix Marseille
515 University; Prof. Stefano Utili of Newcastle University; Dr. Mori Utsuno of
516 Kajima corporation; Dr. Yishu Wang of Hohai University.

517 In addition, we appreciate the TC105 international committee for sup-
518 porting the international activity, especially for advisement of the core mem-
519 bers on the advertisement and invitation of the participants. Finally, we
520 thank to the TC105 Japanese domestic committee members for their active
521 discussion on the design of the experiments and simulations in the round
522 robin test.

523 **References**

524 Angelidakis, V., Nadimi, S., Utili, S., 2021. SHape analyser for particle engi-
525 neering (SHAPE): Seamless characterisation and simplification of particle
526 morphology from imaging data. *Computer Physics Communications* 265,
527 107983.

528 Berre, I., Boon, W.M., Flemisch, B., Fumagalli, A., Gläser, D., Keilegavlen,

- 529 E., Scotti, A., Stefansson, I., Tatomir, A., Brenner, K., Burbulla, S., De-
530 vloo, P., Duran, O., Favino, M., Hennicker, J., Lee, I.H., Lipnikov, K.,
531 Masson, R., Mosthaf, K., Nestola, M.G.C., Ni, C.F., Nikitin, K., Schädle,
532 P., Svyatskiy, D., Yanbarisov, R., Zulian, P., 2021. Verification bench-
533 marks for single-phase flow in three-dimensional fractured porous media.
534 *Advances in Water Resources* 147, 103759.
- 535 Chen, J., Furuichi, M., Nishiura, D., 2020. Discrete element simulation and
536 validation of a mixing process of granular materials. *Materials* 13.
- 537 Chen, J., Kitamura, A., Barbieri, E., Nishiura, D., Furuichi, M., 2022. Ana-
538 lyzing effects of microscopic material parameters on macroscopic mechani-
539 cal responses in underwater mixing using discrete element method. *Powder*
540 *Technol.* 401, 117304.
- 541 Cheng, Y.P., Nakata, Y., Bolton, M.D., 2003. Discrete element simulation
542 of crushable soil. *Géotechnique* 53, 633–641.
- 543 Chew, K., Chiaro, G., Vinod, J.S., A., T., Allulakshmi, K., 2022. Direct
544 shear behavior of gravel-rubber mixtures: discrete element modeling and
545 microscopic investigations. *Soils and Foundations* (in press) .
- 546 Cundall, P.A., 1971. A computer model for simulating progressive, large-
547 scale movement in blocky rock system. *Proceedings of the International*
548 *Symposium on Rock*, Nancy, France 2, 129–136.
- 549 Cundall, P.A., Strack, O.D.L., 1979. A discrete numerical model for granular
550 assemblies. *Géotechnique* 29, 47–65.

- 551 Dadvand, P., Rossi, R., Gil, M., Martorell, X., Cotela, J., Juanpere, E., Idel-
552 sohn, S.R., Oñate, E., 2013. Migration of a generic multi-physics frame-
553 work to HPC environments. *Computers & Fluids* 80, 301–309.
- 554 Dadvand, P., Rossi, R., Oñate, E., 2010. An object-oriented environment
555 for developing finite element codes for multi-disciplinary applications.
556 *Archives of Computational Methods in Engineering* 17, 253–297.
- 557 Duriez, J., Darve, F., Donzé, F.V., 2011. A discrete modeling-based con-
558 stitutive relation for infilled rock joints. *International Journal of Rock*
559 *Mechanics and Mining Sciences* 48, 458–468.
- 560 Furuichi, M., Nishiura, D., Asai, M., Hori, T., 2017. The first real-scale
561 DEM simulation of a sand-box experiment using 2.4 billion particles. The
562 International Conference for High Performance Computing, Networking,
563 Storage and Analysis URL: [https://sc17.supercomputing.org/SC17%](https://sc17.supercomputing.org/SC17%20Archive/tech_poster/tech_poster_pages/post113.html)
564 [20Archive/tech_poster/tech_poster_pages/post113.html](https://sc17.supercomputing.org/SC17%20Archive/tech_poster/tech_poster_pages/post113.html).
- 565 Harris, R.A., Barall, M., Aagaard, B., Ma, S., Roten, D., Olsen, K., Duan,
566 B., Liu, D., Luo, B., Bai, K., Ampuero, J., Kaneko, Y., Gabriel, A., Duru,
567 K., Ulrich, T., Wollherr, S., Shi, Z., Dunham, E., Bydlon, S., Zhang, Z.,
568 Chen, X., Somala, S.N., Pelties, C., Tago, J., Cruz-Atienza, V.M., Kozdon,
569 J., Daub, E., Aslam, K., Kase, Y., Withers, K., Dalguer, L., 2018. A suite
570 of exercises for verifying dynamic earthquake rupture codes. *Seismological*
571 *Research Letters* 89, 1146–1162.
- 572 Harris, R.A., Barall, M., Andrews, D.J., Duan, B., Ma, S., Dunham, E.M.,
573 A. Gabriel, A., Kaneko, Y., Kase, Y., Aagaard, B.T., Oglesby, D.D.,

- 574 P. Ampuero, J., Hanks, T.C., Abrahamson, N., 2011. Verifying a com-
575 putational method for predicting extreme ground motion. *Seismological*
576 *Research Letters* 82, 638–644.
- 577 Horrillo, J., Grilli, S.T., Nicolsky, D., Roeber, V., Zhang, J., 2015. Perfor-
578 mance benchmarking tsunami models for NTHMP’s inundation mapping
579 activities. *Pure and Applied Geophysics* 172, 869–884.
- 580 Irazábal, J., Salazar, F., Oñate, E., 2017. Numerical modelling of granular
581 materials with spherical discrete particles and the bounded rolling friction
582 model. application to railway ballast. *Computers and Geotechnics* 85,
583 220–229.
- 584 Itasca Consulting Group, Inc., 2021. PFC — Particle Flow Code, Minneapo-
585 lis: Itasca.
- 586 Jiang, M., Liu, A., Wang, H., Lu, G., Li, L., 2020. An empirical strength
587 criterion for deep rock incorporating the effect of fracture intensity using
588 distinct element method. *IOP Conf. Ser.: Earth Environ. Sci.* 570, 022060.
- 589 Jiang, M., Shen, Z., Wang, J., 2015. A novel three-dimensional contact model
590 for granulates incorporating rolling and twisting resistances. *Computers*
591 *and Geotechnics* 65, 147–163.
- 592 Kanno, H., Moriguchi, S., Hayashi, S., Terada, K., 2021. A computational
593 design optimization method for rockfall protection embankments. *Engi-
594 neering Geology* 284, 105920.

- 595 Kikkawa, N., Hori, T., Itoh, K., Mitachi, T., 2013. Study on a determina-
596 tion manner of discrete element method parameters in a bonded granular
597 material. *Japanese Geotechnical Journal (in Japanese)* 8, 221–237.
- 598 Kloss, C., Goniva, C., Hager, A., Amberger, S., Pirker, S., 2012. Models,
599 algorithms and validation for opensource DEM and CFD–DEM. *Progress*
600 *in Computational Fluid Dynamics, an International Journal* 12, 140–152.
- 601 Kono, A., 2018. Validation of numerical simulation using 3d-discrete element
602 ballasted track model, in: *Computers in Railways XVI : Railway Engineer-*
603 *ing Design and Operation*, WIT Press, Southampton UK. pp. 169–177.
- 604 Lin, Z.Y., Wang, Y.S., Tang, C.S., Cheng, Q., Zeng, H., Liu, C., Shi, B.,
605 2021. Discrete element modelling of desiccation cracking in thin clay layer
606 under different basal boundary conditions. *Computers and Geotechnics*
607 130, 103931.
- 608 Matsushima, T., Saomoto, H., 2002. Discrete element modeling for
609 irregularly-shaped sand grains, in: *NUMGE 2002. 5th European Confer-*
610 *ence Numerical Methods in Geotechnical Engineering*, pp. 239–246.
- 611 Nakase, H., Iwamoto, T., Cao, G., Tabei, K., Sakaguchi, H., Matsushima, T.,
612 2017. Reproduction analysis of actual slope collapse and parametric study
613 for evacuation of the deposit volume by a simple model of distinct element
614 method. *Journal of Japan Society of Civil Engineers, Ser. A1 (Structural*
615 *Engineering & Earthquake Engineering (SE/EE)) (in Japanese)* 73, I.694–
616 I.703.

- 617 Nakata, Y., Moriguchi, S., Kajiyama, S., Kido, R., Kikkawa, N., Saomoto,
618 H., Takano, D., Higo, Y., 2022. Experimental data of 3D printed granular
619 material for verification of discrete element modelling simulation. *Soils and*
620 *Foundations* (in press) .
- 621 Nishiura, D., Furuichi, M., Sakaguchi, H., 2021. Real-scale DEM simulations
622 on the fault evolution process observed in sandbox experiments. *Adv.*
623 *Powder Technol.* 32, 4432–4441.
- 624 Nishiura, D., Sakai, H., Aikawa, A., Tsuzuki, S., Sakaguchi, H., 2018. Novel
625 discrete element modeling coupled with finite element method for investi-
626 gating ballasted railway track dynamics. *Computers and Geotechnics* 96,
627 40–54.
- 628 O’Sullivan, C., 2011. *Particulate discrete element modelling: a geomechanics*
629 *perspective*. CRC Press.
- 630 Otsubo, M., O’Sullivan, C., 2018. Experimental and DEM assessment of the
631 stress-dependency of surface roughness effects on shear modulus. *Soils and*
632 *Foundations* 58, 602–614.
- 633 Otsubo, M., O’Sullivan, C., Hanley, K.J., Sim, W.W., 2017. The influence
634 of particle surface roughness on elastic stiffness and dynamic response.
635 *Géotechnique* 67, 452–459.
- 636 Sakaguchi, H., Nishiura, D., 2009. Development of hyper intelligent discrete
637 element method (HiDEM) and its application for science and industry.
638 JAMSTEC Report of Research and Development (in Japanese) 2009, 201–
639 209.

640 Sandia National Laboratories, 2001. LAMMPS molecular dynamics simula-
641 tor. <https://www.lammps.org/index.html>. Accessed: 2021-11-4.

642 Shimizu, H., Murata, S., Ishida, T., 2011. The distinct element analysis for
643 hydraulic fracturing in hard rock considering fluid viscosity and particle
644 size distribution. *International Journal of Rock Mechanics and Mining*
645 *Sciences* 48, 712–727.

646 Smilauer, V., Angelidakis, V., Catalano, E., Caulk, R., Chareyre, B.,
647 Chèvremont, W., Dorofeenko, S., Duriez, J., Dyck, N., Elias, J., Er, B., Eu-
648 litz, A., Gladky, A., Guo, N., Jakob, C., Kneib, F., Kozicki, J., Marzougui,
649 D., Maurin, R., Modenese, C., Pekmezi, G., Scholtès, L., Sibille, L., Stran-
650 sky, J., Sweijen, T., Thoeni, K., Yuan, C., 2021. Yade documentation.
651 The Yade Project. URL: <https://doi.org/10.5281/zenodo.5705394>,
652 doi:10.5281/zenodo.5705394.

653 TC105 Japanese domestic committee, 2020. Round robin test of angle of re-
654 pose (AOR). <http://geotech.civil.yamaguchi-u.ac.jp/tc105/>. Ac-
655 cessed: 2021-9-21.

656 Thompson, A.P., Aktulga, H.M., Berger, R., Bolintineanu, D.S., Brown,
657 W.M., Crozier, P.S., in 't Veld, P.J., Kohlmeyer, A., Moore, S.G., Nguyen,
658 T.D., Shan, R., Stevens, M.J., Tranchida, J., Trott, C., Plimpton, S.J.,
659 2022. LAMMPS - a flexible simulation tool for particle-based materials
660 modeling at the atomic, meso, and continuum scales. *Computer Physics*
661 *Communications* 271, 108171.

662 Tsuji, K., Asai, M., Konishi, Y., Oomine, S., 2019. Sph-Dem coupling simu-

- 663 lation with a liquid bridge force for the representation of ground collapse
664 phenomenon. *Journal of Japan Society of Civil Engineers, Ser. A2 (Applied*
665 *Mechanics (AM)) (in Japanese)* 75, I.203–I.213.
- 666 Yamaguchi, A., Maeda, K., Matsuda, T., Takagi, K., 2017. Fluidity and
667 pore water pressure variation in the sandy ground induced by surface layer
668 flow using dem-cfd. *Journal of Japan Society of Civil Engineers Ser B2*
669 *(Coastal Engineering) (in Japanese)* 73, I.517–I.522.
- 670 Yu, Y., Cheng, Y.P., Xu, X., Soga, K., 2016. Discrete element modelling of
671 methane hydrate soil sediments using elongated soil particles. *Computers*
672 *and Geotechnics* 80, 397–409.
- 673 Zeghal, M., El Shamy, U., 2004. A continuum-discrete hydromechanical anal-
674 ysis of granular deposit liquefaction. *International Journal for Numerical*
675 *and Analytical Methods in Geomechanics* 28, 1361.